Phase behaviour of quasicrystal forming systems of core-corona particles

Harini Pattabhiraman and Marjolein Dijkstra

Citation: The Journal of Chemical Physics **146**, 114901 (2017); doi: 10.1063/1.4977934
View online: http://dx.doi.org/10.1063/1.4977934
View Table of Contents: http://aip.scitation.org/toc/jcp/146/11
Published by the American Institute of Physics

Phase behaviour of quasicrystal forming systems of core-corona particles

Harini Pattabhiraman[a] and Marjolein Dijkstra[b]
Soft Condensed Matter, Debye Institute for Nanomaterials Science, Department of Physics, Utrecht University, Princetonplein 5, 3584 CC Utrecht, The Netherlands

(Received 11 November 2016; accepted 10 February 2017; published online 15 March 2017)

Using Monte Carlo simulations and free-energy calculations, we study the phase behaviour of a two-dimensional system of particles interacting with a hard core of diameter σ_{HD} and a repulsive square shoulder potential. The interest in this system lies in the formation of quasicrystals of different symmetries at specific square-shoulder widths δ as previously reported by Dotera *et al.* [Nature **506**, 208 (2014)]. However, an insight into other possible periodic phases formed in these systems and the thermodynamic stability of both the periodic and quasicrystal phases is yet to be addressed. Here, we study the phase behaviour and map out the phase diagrams for three different shoulder widths $\delta = 1.27\sigma_{HD}, 1.40\sigma_{HD}$, and $1.60\sigma_{HD}$, where octadecagonal, dodecagonal, and decagonal quasicrystals were previously reported. In addition, we verify the thermodynamic stability of these quasicrystals with respect to their periodic approximants. In general, we find that the system at all three shoulder widths forms hexagonal phases in two distinct density ranges due to the two characteristic length scales in the interaction potential. Further, we find that the dodecagonal and octadecagonal quasicrystals are stable in between two crystal phase regimes. In contrast, the decagonal quasicrystal is not bounded by a low-density crystal phase regime due to the lower density of this quasicrystal. From the free-energy calculations, we find indications that the decagonal and dodecagonal quasicrystals are thermodynamically stable with respect to their approximants, and the octadecagonal quasicrystal is stabilised by a configurational entropy contribution. *Published by AIP Publishing.* [http://dx.doi.org/10.1063/1.4977934]

I. INTRODUCTION

Despite a huge interest in recent years in the synthesis of novel colloidal building blocks with different shapes and inter-particle interactions for obtaining new structures, it is intriguing to note that very simple particle systems can still exhibit surprisingly rich phase behaviour with unexpected novel phases. For instance, a simple architecture consisting of spherical particles with a rigid core and a squishy corona has been used as a simple model system to explain quasicrystals in soft matter.[1] Quasicrystals are materials that exhibit long-range positional order without translational periodicity.[2] This architecture emulates either spherical dendrite micelles consisting of a rigid aromatic core with a deformable shell of alkyl chains[3] or block copolymer micelles consisting of a micellar core of hydrophobic polymer surrounded by a large shell of hydrophilic polymer blocks.[4–8] Computational studies of soft-matter quasicrystals essentially involve mimicking this core-corona architecture using a suitable inter-particle interaction potential. In two-dimensional systems, this includes attractive potentials like Lennard-Jones-Gauss,[9–11] square-well,[12,13] flat-well,[14] and three-well oscillating[15] interactions and purely repulsive interactions like the linear ramp,[16] square-shoulder,[17,18] repulsive shoulder,[18] and various forms of exponential[19–21] interactions.

A comprehensive exploration for quasicrystals in a two-dimensional system with an inter-particle potential consisting of a hard core and a repulsive square shoulder was performed by Dotera *et al.*[17] They identified six quasicrystals of various symmetries in the density and shoulder width parameter space. These quasicrystals were identified as low temperature phases formed by cooling a hexagonal phase from a high temperature. A similar analysis was more recently carried out by Schoberth *et al.*[18] wherein they also analysed, in addition to the above mentioned square-shoulder system, a system where the repulsive interaction within the corona was not constant. Similar to the procedure adopted by Dotera *et al.*, Schoberth *et al.* identified the low temperature phases formed at each point in the density-shoulder width parameter space. This also included periodic crystals of square and hexagonal symmetry. These fundamental studies pave the way for a number of questions regarding the overall phase behaviour of these systems, which includes the presence of other periodic crystals as well as the thermodynamic stability of all of these phases.

By studying the overall phase behaviour of these systems, we direct our attention to the formation and stability of various periodic crystals and quasicrystals in core-corona systems. The formation of soft-matter quasicrystals is aided by the presence of two characteristic length scales in the system;[1,22–25] and the formation of periodic crystals in core-corona systems is interesting due to the formation of lattices exclusively in core-corona systems, such as the A15 lattice

[a]h.pattabhiraman@uu.nl
[b]m.dijkstra@uu.nl

in three-dimensional system[26,27] and the square or rhombus lattices in two-dimensional systems.[9,16,28] We wish to explore the formation of such uniquely formed periodic crystals in two-dimensional core-corona systems. Further, to determine the stable phases in the system, we calculate the free energy of all identified phases and map out the phase diagram. The presence of quasicrystals in the system complicates the free-energy calculation in a number of ways: First, a suitable reference state with known free energy from which we can construct a thermodynamic integration path to the quasicrystal in the system of our interest is not known. Second, the configurational entropy of the quasicrystal needs to be incorporated, but sampling over all of its possible distinct configurations is non-trivial. Third, assessing the stability of quasicrystal would involve the inclusion of their approximants.[29–32] Approximants are periodic crystals that approximate the structure of a quasicrystal on a local level, i.e., they have identical local tiling structure as the quasicrystal.[29–31,33] The higher stability of the quasicrystal is favoured by its configurational entropy accounting for the number of distinct configurations,[32] while the approximant is stabilised by its lower energy and more efficient packing.[30,31,34] And finally, the relative stability of quasicrystals and their approximants is dependent on the system under study and needs to be exclusively addressed for each system.

In this work, we address the above points of interest by studying the phase behaviour and mapping out the phase diagram for a two-dimensional system of hard disks interacting with a repulsive square-shoulder potential at three different shoulder widths $\delta = 1.27\sigma_{HD}$, $1.40\sigma_{HD}$, and $1.60\sigma_{HD}$ for which octadecagonal, dodecagonal, and decagonal quasicrystals were reported previously.[17] We identify the various phases formed in the system by using Monte Carlo (MC) simulations. We calculate the free energy of the periodic crystal phases using the Frenkel-Ladd method, and we employ different methods for calculating the free energy of the high-density dodecagonal and octadecagonal quasicrystals, and the low-density decagonal quasicrystals. For the high-density quasicrystals, where the movement of particles is restricted, we perform a thermodynamic integration to a non-interacting Einstein crystal, i.e., the Frenkel-Ladd method,[35,36] and account for the configurational entropy by using an expression from literature.[37] For the low-density quasicrystal, where particle movements need to be accounted, the reference state is a system of non-interacting particles pinned to their respective positions by an attractive linear well (Schilling-Schmid method[38,39]). Eventually, we map out the phase diagrams in the temperature-density plane at each of the three shoulder widths. We have already reported the phase diagram for the system with a shoulder width of $\delta = 1.40\sigma_{HD}$ in a preliminary account,[40] where we exclusively addressed the issue of the relative stability of the dodecagonal quasicrystal with respect to various approximants. In this work, we address the general phase behaviour at all three shoulder widths.

The paper is organised as follows. In Sec. II, we present our model and the methods that we employ to map out the phase diagram. The results are presented in Sec. III, and we end with some conclusions in Sec. IV.

II. METHODS

A. Model and simulations

In this paper, we study a two-dimensional system of hard disks with a soft corona, which is represented by a repulsive square-shoulder potential.[17,40] The inter-particle potential of this hard-core square shoulder (HCSS) system, $V_{\mathrm{HCSS}}(r)$, is the sum of a hard-disk potential $V_{\mathrm{HD}}(r)$ and a square-shoulder potential $V_{\mathrm{SS}}(r)$, i.e.,

$$V_{\mathrm{HCSS}}(r) = V_{\mathrm{HD}}(r) + V_{\mathrm{SS}}(r),$$

where

$$V_{\mathrm{HD}}(r) = \begin{cases} \infty, & r \le \sigma_{HD} \\ 0, & r > \sigma_{HD} \end{cases} \tag{1}$$

and

$$V_{\mathrm{SS}}(r) = \begin{cases} \epsilon, & r \le \delta \\ 0, & r > \delta. \end{cases} \tag{2}$$

Here σ_{HD} denotes the particle diameter, r is the distance between the centre-of-masses of two particles, and δ and ϵ are, respectively, the width and height of the square shoulder. Fig. 1 shows a schematic representation of this pair potential, where the hard core and square shoulder are represented by the dark and light red circles.

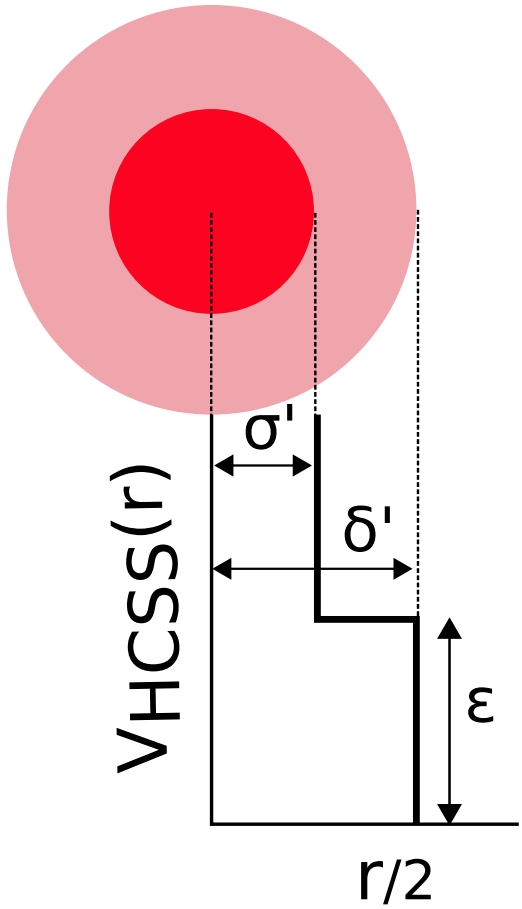

FIG. 1. Schematic representation of the hard-core square shoulder (HCSS) potential, $V_{\mathrm{HCSS}}(r)$, as a function of the semi inter-particle distance $r/2$. $\sigma' = \sigma_{HD}/2$ and $\delta' = \delta/2$ are, respectively, the radius of the particle and the square shoulder.

We study the phase behaviour of the HCSS system at three different shoulder widths. Phases with 10-, 12-, and 18-fold symmetry, namely, decagonal, dodecagonal, and octadecagonal quasicrystals, were reported previously for shoulder width values of $\delta = 1.60\sigma_{HD}$, $1.40\sigma_{HD}$, and $1.27\sigma_{HD}$, respectively.[17,18] These shoulder widths are close to the optimal irrational ratios that promote the formation of quasicrystals, viz., $2\cos 36° \approx 1.618$, $2\cos 45° \approx 1.414$, and $2\cos 50° \approx 1.286$ as explained in Ref. 17. In order to facilitate comparisons with earlier studies, we use the values as employed by Dotera *et al.* instead of employing the optimal ones given above.

We perform Monte Carlo (MC) simulations in the canonical (NVT) and isothermal-isobaric (NPT) ensemble, where the number of particles N, the temperature T, and the volume V, or pressure P, respectively, are fixed. The particles are simulated in a rectangular box of area A under periodic boundary conditions. We introduce the following reduced (dimensionless) quantities: temperature $T^* = k_BT/\epsilon$, pressure $P^* = \beta P\sigma_{HD}^2$, and density $\rho^* = N\sigma_{HD}^2/A$, where $\beta = 1/k_BT$ is the inverse temperature with k_B the Boltzmann constant. A system size of $N = 4900$ is used in the NVT-MC simulations.

B. Structural analysis

To qualitatively analyse the structures that the system adopts under various conditions, we calculate their corresponding polygonal tilings by drawing the bonds between the neighbouring particles. Decoding quasicrystals as random tilings of polygons is common practice. Commonly known examples of such tilings include the square-triangle tiling of a dodecagonal quasicrystal[37,41] and the polygon tiling of a decagonal quasicrystal consisting of regular and nonconvex decagons, nonagons, hexagons, and pentagons.[9,32,42] Dotera *et al.* proposed an alternative overview of these tilings by deconstructing each polygon as combinations of two of the four possible Robinson triangles that can be constructed by three particles. In this work, we use the formerly stated more widely used multi-polygonal tiling descriptions. This helps in correlating the quasicrystals and approximants to previous literatures as explained separately for each quasicrystal in Sec. III. To summarize, the dodecagonal quasicrystal consists of a square-triangle tiling, the octadecagonal quasicrystal consists of a rhombus-triangle tiling, and the decagonal quasicrystal consists of a tiling consisting of regular and nonconvex polygons.

For further quantitative analysis, we calculate the average bond orientational order (BOO) parameter of the system and the local environment of each particle. The average BOO parameter χ_m is defined as[43]

$$\chi_m = \left\langle \left| \frac{1}{N_B(i)} \sum_{j=1}^{N_B(i)} \exp(im\theta_{\mathbf{r}_{ij}}) \right|^2 \right\rangle, \tag{3}$$

where m is the symmetry of interest, $N_B(i)$ is the number of neighbours of particle i, with particle j defined to be a neighbour if $r_{ij} = |\mathbf{r}_i - \mathbf{r}_j| \leq \delta$, $\mathbf{r}_i$ and $\mathbf{r}_j$ are the positions of particles i and j, and $\theta_{\mathbf{r}_{ij}}$ is the angle between the centre-of-mass distance vector $\mathbf{r}_{ij}$ and an arbitrary axis.

The local particle environment (LPE) in dodecagonal quasicrystals is composed of the various possible arrangements of squares and triangles. This includes environments of only triangles (Z) or squares ($A15$) and a combination of the two. Mixed arrangements of squares and triangles primarily result in two five-particle coordinated environments, which are termed as H and σ, in analogy to the Frank-Kasper phases.[44] An overview of these LPEs is given in Figure 2. We also identify the same LPEs for the octadecagonal quasicrystal in which the squares are replaced by rhombi.

C. Phase diagram construction

Obtaining the phase diagram is essentially a three step process. First, the equation of state (EOS), i.e., the bulk pressure P^* as a function of density ρ^*, is constructed. This is done by measuring the equilibrium density at a fixed pressure in a NPT-MC simulation and by subsequently changing the pressure in a step-wise manner. Compression runs are always started from a disordered isotropic fluid (FL) phase and expansion runs from a crystal or quasicrystal phase with symmetries according to the system under study. We then determine the free energy as a function of density by integrating the respective EOS as will be described in Section II D. Finally, a common tangent construction is employed to the free-energy curves of all phases to determine the thermodynamically stable phases.

D. Free-energy calculations

For all observed phases, viz., fluid, crystal, and quasicrystal, we calculate the dimensionless Helmholtz free energy per particle, $f = \beta F/N$, as a function of density ρ by thermodynamically integrating the equation of state from a reference density, ρ_o, for which the free energy is known for the respective phase

$$f(\rho) = f(\rho_o) + \int_{\rho_o}^{\rho} \frac{\beta P(\rho')}{\rho'^2} d\rho'. \tag{4}$$

In order to determine the Helmholtz free energy at the reference density ρ_o, we employ another thermodynamic integration

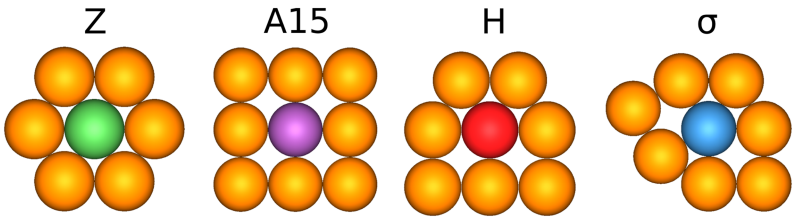

FIG. 2. Overview of the Z, $A15$, H, and σ local particle environments (LPEs) in dodecagonal and octadecagonal quasicrystals. Particles with LPEs other than these are coloured orange.

using a reference system that depends on the bulk phase of interest.

1. Fluid phases

For the fluid phase, the free energy at the reference density is calculated by constructing a reversible path from the HCSS system to the hard-disk fluid at the same density.[35,36] To do so, we introduce an auxiliary potential energy function

$$\beta U_{SS}(\gamma) = \sum_{i<j}^{N} \beta V_{HD}(r_{ij}) + \gamma \sum_{i<j}^{N} \beta V_{SS}(r_{ij}) \tag{5}$$

that linearly interpolates between the hard-disk system at $\gamma = 0$ and the HCSS system at $\gamma = 1$, where γ denotes the linear coupling parameter. The free energy of the HCSS system is then determined by

$$f(\rho) = f_{HD}(\rho) + \frac{1}{N}\int_{\gamma=0}^{\gamma=1} d\gamma \left\langle \frac{\partial \beta U_{SS}(\gamma)}{\partial \gamma} \right\rangle, \tag{6}$$

where $f_{HD}(\rho)$ is the free energy of the hard-disk fluid and is calculated using the following expression by Santos *et al.*:[45]

$$f_{HD}(\rho) = \left[\ln\left(\rho\Lambda^2\right) - 1\right] - \frac{\ln\left(1 - \frac{\eta}{\eta_m}\right)}{2(1-\eta_m)} + \frac{(2\eta_m - 1)\ln\left(1 - \frac{2\eta_m - 1}{\eta_m}\eta\right)}{2(1-\eta_m)}, \tag{7}$$

where $\eta = \pi\sigma_{HD}^2 N/4A$ denotes the packing fraction and η_m corresponds to the packing fraction of the close-packed crystal phase. The first term in Eq. (7) represents the free energy per particle of an ideal gas in two dimensions.

2. Periodic crystal phases

The free energy of the periodic crystal phases as well as the periodic approximants is calculated using the Frenkel-Ladd method where an Einstein crystal is used as the reference state.[35,36,46,47] The Einstein crystal is an ideal lattice where the particles are fixed so strongly to their lattice positions by harmonic springs that they do not interact with each other. The lattice positions of the particles are taken to be that of the equilibrium positions of the crystal structure under consideration. A reversible path is then constructed from the crystal of interest to the Einstein crystal in two steps. First, the SS potential is switched off by using Eq. (5) and changing γ from 1 to 0. Then, the harmonic springs are switched on using another auxiliary potential energy function, while the hard-core interactions remain unaffected. This potential energy function reads

$$\beta U(\lambda) = \sum_{i<j}^{N} \beta V_{HD}(r_{ij}) + \lambda \sum_{i=1}^{N} \frac{(\mathbf{r}_i - \mathbf{r}_{i,o})^2}{\sigma_{HD}^2}, \tag{8}$$

where $\mathbf{r}_{i,o}$ and $\mathbf{r}_i$ are, respectively, the equilibrium and instantaneous position of particle i. These springs are switched on by increasing their dimensionless spring constant λ, from zero to a value λ_{max}, where the particles are so strongly confined to their ideal lattice positions that they move independently of each other. Hence, the free energy of the crystal can be approximated to that of the Einstein crystal. Consequently, the free energy of this crystal at a certain density for a d-dimensional system is calculated as[46]

$$f_{HC}(\rho) = f_{\mathrm{Ein}} - \Delta f_{CM} + \frac{\ln\rho}{N} - \frac{d}{2N}\ln N - \frac{d}{2N}\ln\frac{\lambda_{\max}}{\pi}, \tag{9}$$

where the first term is the free energy of a non-interacting Einstein crystal given by

$$f_{\mathrm{Ein}} = -\frac{d}{2}\ln\frac{\pi}{\lambda_{\max}} \tag{10}$$

and the second term is the free-energy difference between the solid under consideration and the Einstein crystal

$$\Delta f_{CM} = \int_{\ln c}^{\ln(\lambda_{\max}+c)} d[\ln(\lambda + c)](\lambda + c) \times \left\langle \frac{1}{N}\sum_{i=1}^{N} \frac{(\mathbf{r}_i - \mathbf{r}_{i,o})^2}{\sigma_{HD}^2} \right\rangle_{\lambda} \tag{11}$$

with $c = 1/\left\langle \frac{1}{N}\sum_{i=1}^{N} \frac{(\mathbf{r}_i - \mathbf{r}_{i,o})^2}{\sigma_{HD}^2} \right\rangle_{\lambda\to 0}$. The other terms in Eq. (9) denote the difference between solids with constrained and unconstrained centers of mass. Ultimately, the free energy of a crystal interacting with a HCSS potential is determined as

$$f(\rho) = f_{HC}(\rho) + \frac{1}{N}\int_{\gamma=0}^{\gamma=1} d\gamma \left\langle \frac{\partial \beta U_{SS}(\gamma)}{\partial \gamma} \right\rangle. \tag{12}$$

3. Quasicrystal phases

We categorise the quasicrystals in this study into two classes, namely, the high-density and the low-density quasicrystals. Quasicrystals obtained in our simulations that can be described by a random tiling of regular polygons alone are hereby called high-density quasicrystals. This includes the dodecagonal quasicrystal with a square-triangle tiling and octadecagonal quasicrystal with a rhombus-triangle tiling. On the other hand, decagonal quasicrystals consisting of combinations of regular and convex polygons are referred to as low-density quasicrystals. The methods we use for calculating the free energies of these high- and low-density quasicrystals are different. In the case of the high-density quasicrystal, the movements of the particles are restricted, and we can therefore use a representative "ideal lattice" for calculating the free energy as in case of the Frenkel-Ladd method.[35] In contrast, the particles in the low-density quasicrystal are highly mobile and can thus not be represented by an "ideal lattice." Therefore, we employ the method proposed by Schilling and Schmid for arbitrary fluids and disordered solids.[38,39] It is worth mentioning here that we compared the free energy as obtained by using these two methods for the high-density dodecagonal quasicrystal at different densities and temperatures. The difference between the free energies obtained using the Frenkel-Ladd and the Schilling-Schmid methods was on the order of the statistical error of the free-energy calculations in these methods. We use the Frenkel-Ladd method for the high-density quasicrystals as it is computationally less intensive than the Schilling-Schmid method.

For the high-density quasicrystals, we first calculate the free energy using the Frenkel-Ladd method[35] and then add a configurational entropy contribution associated with the

number of distinct random-tiling configurations. The entropy correction is necessary because the Einstein crystal, which is employed as the reference state, does not account for the configurational entropy of the system. In order to obtain an estimate of the configurational entropy, we consider the random-tiling model of polygons. The dodecagonal (or octadecagonal) quasicrystal results from a random tiling of triangles and squares (rhombi).[17] The configuration resulting in maximum entropy and thus, the formation of quasicrystals, is obtained at equal area fractions of triangles and squares (or rhombi).[17,37] For such a configuration of triangles and squares, two different values are reported in the literature for the entropy per unit area S_{config}/k_BA. A value of $S_{\text{config}}/k_BA = 0.129\,34$ was calculated by Widom[37] by solving the Bethe ansatz for the square-triangle random-tiling model for infinitely large systems,[37,48,49] and a value of $S_{\text{config}}/k_BA = 0.131\,37$ was estimated by Oxyborrow and Henley[50] using Monte Carlo simulations. In this work, we use the more conservative value obtained by Widom. We wish to remark here that a negligible effect of system size on this value was reported for system sizes larger than $N = 153$.[37] Here, we use a system consisting of 209 particles. Further, we employ the same value of configurational entropy for both the dodecagonal and the octadecagonal quasicrystal. We postulate that as the configurational entropy of a dodecagonal square-triangle[49] and an octagonal rectangle-right-angled triangle[51] random tilings is similar, then a similar value will also apply to the octadecagonal rhombus-triangle tiling. We, however, note here that we expect a higher configurational entropy for the octadecagonal rhombus-triangle tiling and an even higher one for the octagonal rectangle-right-angled triangle tiling because of the lower symmetry of the rhombus, rectangle, and right-angled triangle. Further, it is good to note here that this analytical description of the configurational entropy considers a perfect random tiling, where all configurations are equally probable. However, this might not be true for the HCSS system, where the probability of finding a certain tiling will also depend on its potential energy and vibrational entropy. The potential energy of the system is determined by the pair interactions and the latter by the number of configurations that the particles can explore while moving around their lattice positions. Thus, the value used here is an upper bound for the configurational entropy of the HCSS system consisting of a square-triangle random tiling. However, as mentioned above, we expect a higher entropy for the HCSS system consisting of a rhombus-triangle tiling.

For the low-density quasicrystal, the free energy is calculated using the method proposed by Schilling and Schmid.[38,39] As this method allows the sampling of distinct configurations, we do not add an additional configurational entropy term. However, this method does not effectively sample the discrete phason flips in the structure, and thus, underestimates the configurational entropy. In this method, the reference state consists of a system of non-interacting particles that are pinned by a local attractive linear well potential to their respective reference positions as described by

$$\beta U_{LW}(\omega) = \omega \sum_{i}^{N} \Phi(|\mathbf{r}_i - \mathbf{r}_i^0|/r_c), \tag{13}$$

where ω is the absolute well depth, $\mathbf{r}_i$ and $\mathbf{r}_i^0$ are the positions of particle i and its corresponding well, respectively, r_c is the radius of the well, and $\Phi(x) = x - 1$ for $x < 1$ or 0 for $x \geq 1$. In this study, the well radius r_c is taken to be twice the particle diameter σ_{HD}.

The free energy of this reference system can be analytically calculated

$$f_{ref}(\rho) = \ln(\rho\Lambda^d) - 1 - \ln\left(1 + \frac{V_o}{V} g(\omega)\right), \tag{14}$$

where V_o is the volume of a sphere of radius r_c and

$$g(\omega) = \frac{d}{\omega^d}\left(e^{\omega} - \sum_{k=0}^{d} \frac{\omega^k}{k!}\right) \tag{15}$$

for a d-dimensional system.

The HCSS system is obtained from the reference system composed of non-interacting pinned particles by a three-step thermodynamic integration process consisting of (i) switching on the hard-core interactions of the particles, (ii) switching on the square-shoulder interactions of the particles, and (iii) switching off the linear well potentials of the particles. The hard-core interactions are switched on by using the following potential:[52]

$$U_{HD}(r_{ij}, \alpha) = \begin{cases} \alpha\left[1 - 0.9\left(\frac{r_{ij}}{\sigma_{HD}}\right)^2\right], & r_{ij} < \sigma_{HD} \\ 0 & r_{ij} \geq \sigma_{HD}, \end{cases} \tag{16}$$

where $r_{ij} = |\mathbf{r}_i - \mathbf{r}_j|$ with $\mathbf{r}_i$ and $\mathbf{r}_j$ the positions of particles i and j. The square-shoulder interaction is switched on by using the auxiliary potential energy function given in Eq. (5). The free energy of the HCSS system can ultimately be calculated from

$$\begin{aligned} f(\rho) = f_{ref}(\rho) &+ \frac{1}{N}\int_0^{\alpha_{max}} d\alpha \left\langle \frac{\partial \beta U_{HD}}{\partial \alpha} \right\rangle_{\alpha,\gamma=0,\omega_{max}} \\ &+ \frac{1}{N}\int_0^{1} d\gamma \left\langle \frac{\partial \beta U_{SS}}{\partial \gamma} \right\rangle_{\gamma,\alpha_{max},\omega_{max}} \\ &- \frac{1}{N}\int_0^{\omega_{max}} d\omega \left\langle \frac{\partial \beta U_{LW}}{\partial \omega} \right\rangle_{\omega,\alpha_{max},\gamma=1}. \end{aligned} \tag{17}$$

III. RESULTS AND DISCUSSION

In this section, we discuss the phase behaviour of the HCSS system for three different shoulder widths. We present the phase behaviour of the HCSS system at each shoulder width separately. A preliminary account of the phase diagram for shoulder width $\delta = 1.40\sigma_{HD}$ was already presented in Ref. 40, where the focus was on the relative stability of the dodecagonal quasicrystal and four different approximants. Here, we present this phase diagram again for comparison with the phase behaviour at other shoulder widths. In addition, we present information on the general phase behaviour at different temperatures using the equation of states, address the formation of the quasicrystal in terms of the bond orientational order (BOO) parameters, and differentiate between the structures of the quasicrystal and the approximant using their local particle environments (LPEs).

A. Shoulder width $\delta = 1.40\sigma_{HD}$

For a system of HCSS particles with a shoulder width $\delta = 1.40\sigma_{HD}$, a dodecagonal quasicrystal consisting of a random tiling of squares and triangles has been observed in simulations by Dotera *et al.*[17] The dodecagonal quasicrystal (QC12) was reported to form by cooling a high-density hexagonal (HDH) phase of density $\rho^* = 0.98$ to a lower temperature at a constant density in the *NVT* ensemble. In addition, we find in our simulations that the dodecagonal quasicrystal also forms when an isotropic fluid (FL) phase is compressed to a higher density at a constant temperature in the *NPT* ensemble. These transformations can be monitored using the *m*-fold BOO parameter χ_m. In Fig. 3, we show the behaviour of three BOO parameters χ_4, χ_6, and χ_{12}, representing square, hexagonal, and dodecagonal order. In Fig. 3(a), we plot the BOO parameter as a function of temperature T^* during the cooling of the HDH phase at a density of $\rho^* = 0.98$. We observe that the value of χ_6 decreases and the values of χ_4 and χ_{12} increase upon decreasing the temperature. This signals the formation of the QC12. This behaviour of χ_m is due to the formation of local particle environments (LPEs) consisting of *A*15, *H*, and σ at the expense of *Z*. Similarly, Fig. 3(b) shows the BOO parameter as a function of pressure P^* during compression of the FL phase at a temperature $T^* = 0.30$. We observe a discontinuity in χ_{12} with pressure, which points to a first-order phase transition from the fluid to the quasicrystalline phase.

In Fig. 4(a), we show a typical configuration of the random-tiling dodecagonal quasicrystal (QC12) on the top, and its accompanying tiling (left) and diffraction pattern (right) at the bottom as obtained from simulations at $\rho^* = 0.98$ and $T^* = 0.278$ in the *NVT* ensemble. Only the particle cores are shown in the configurations which are coloured according to their LPEs as described in Section II B. The resulting configuration contains defects of primarily pentagonal shape, which are highlighted in the accompanying tiling. In order to verify the nature of the QC12 tiling, we measure the ratio of number of triangles to squares in the tiling. We obtained a value of 2.3, which is close to that of the maximum entropy random tiling $4/\sqrt{3} \approx 2.309$, providing confidence that the additional configurational entropy contribution can be approximated by that of the random square-triangle tiling. In order to eliminate the effect of these defects on the phase diagram calculations, a defect-free configuration was adapted from a non-Stampfli square-triangle approximant.[50] We used the structure given in Fig. 3 of Ref. 50 consisting of 209 particles. This is shown in Fig. 4(b) along with its tiling and diffraction pattern and was used as the initial configuration for the expansion runs of the EOS. In addition, we also show a typical configuration of an approximant crystal (AC12) in Fig. 4(c) together with its tiling and diffraction pattern. An approximant crystal (or crystalline approximant) is a periodic crystal that approximates the structure of a quasicrystal on a local level, i.e., it has a similar local tiling structure.[29–31,33,53] The approximant used here was obtained by repeated vertex substitution of an Archimedean tiling consisting of squares and triangles.[54] The unit cell consists of 56 particles and we use a system consisting of 224 particles in the simulations. We have chosen this type of periodic approximant because of its stability over other approximants and over the *H* and σ phases as shown in our previous simulation study.[40] The colouring of the particles in Fig. 4 according to their LPEs helps in highlighting the structural differences between the QC12 and AC12. The ratio of σ to *H* LPEs is much higher in AC12 in comparison to that in QC12. In other words, the AC12 consists predominantly of σ LPEs, while the QC12 consists of similar fractions of σ and *H* LPEs. Also, the *A*15 LPE, resulting from the presence of neighbouring square tiles, is found only in QC12 and is absent in AC12.

In order to map out the phase diagram, we determine the equations of state (EOSs) by performing compression runs from a disordered isotropic fluid (FL) phase and expansion runs from a crystal phase with square (SQ), and hexagonal symmetry (HDH), an approximant crystal (AC12), and a defect-free dodecagonal quasicrystal (QC12). The EOS calculated at three temperatures $T^* = 0.50$, 0.30, and 0.15 are shown in Fig. 5. At the highest temperature of $T^* = 0.50$, the system exhibits hard-disk-like behaviour with a fluid phase at low densities, a hexagonal phase at sufficiently high densities, and a two-phase coexistence region in between. At the intermediate temperature of $T^* = 0.30$, various high-density solid phases, namely, SQ, QC12, and AC12, start to appear, whereas at the lowest temperature, $T^* = 0.15$, the formation of a low-density hexagonal (LDH) phase bounded by the FL phase is observed.

We now proceed to the calculation of the free energy and the investigation of the relative stability of the various crystal phases, especially that of the quasicrystal and its approximant. The free-energy curves of these phases were

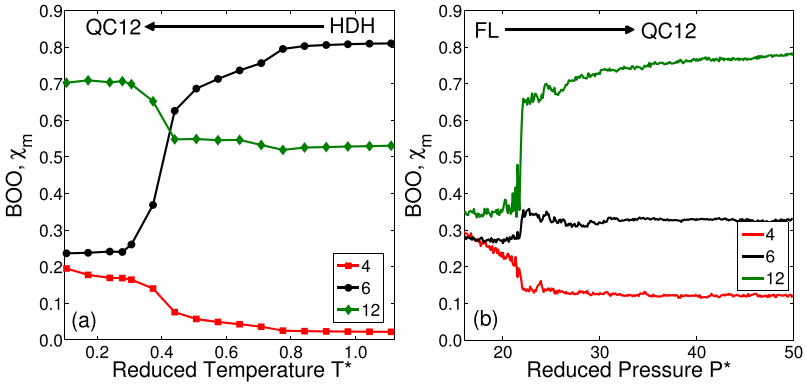

FIG. 3. The *m*-fold bond orientational order (BOO) parameter χ_m as a function of temperature T^* as obtained by cooling a high-density hexagonal (HDH) phase at density $\rho^* = N\sigma_{HD}^2/A = 0.98$ in a simulation of the HCSS system with $\delta = 1.40\sigma_{HD}$ in the *NVT* ensemble (a) and as a function of pressure P^* by compressing a fluid (FL) phase at temperature $T^* = k_BT/\epsilon = 0.30$ in the *NPT* ensemble (b).

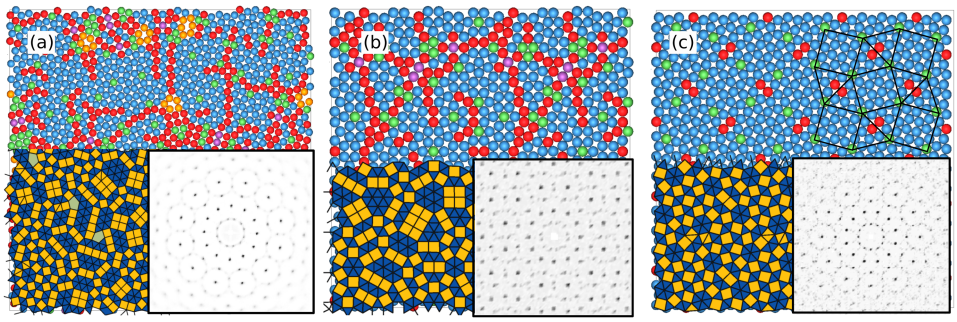

FIG. 4. The random-tiling dodecagonal quasicrystal (QC12) as obtained from simulations (a), a defect-free construction of a random-tiling QC12 (b), and a crystalline approximant (AC12) (c). Each figure displays a typical configuration (top), where the particles are shown in core-only representation and the colours represent the local particle environments (LPEs) as described in Fig. 2, along with its corresponding square-triangle tiling (bottom left) and diffraction pattern (bottom right). The square-triangle tiling formed by the centres of the dodecagons in the approximant in (c) is highlighted.

calculated according to the methods explained in Section II D. To determine the relative stability between the various crystal phases, we construct a common tangent between the different pairs of phases. The common-tangent construction between SQ and HDH at temperature $T^* = 0.10$ is presented in Fig. 6. In Fig. 6, we plot the free energy $\beta F/A - \rho\mu_c + P_c$ as a function of reduced density ρ^* for the following phases: SQ, HDH, AC12, and QC12 without (QC12-woS), and with (QC12-wS) the configurational entropy contribution $S_{\text{config}}/k_B A = 0.129\,34$ as taken from literature.[37] For convenience, we subtract a linear fit $\rho\mu_c - P_c$ from the free-energy curves, where μ_c denotes the bulk chemical potential at the (metastable) SQ-HDH phase coexistence and P_c the corresponding bulk pressure. To identify the relative stability between the QC12-woS and AC12 phases, we take a closer look at the free energy curves of QC12-woS and AC12, as shown in the inset. From Fig. 6, we first note that the minima of the free-energy curves of QC12 and AC12 are below the zero-level showing that the QC12 and AC12 phases are more stable than the SQ-HDH phase coexistence. This magnitude of difference of these curves below the zero level gives the bias for the squares and triangles to mix and to form the QC12, rather than to phase separate into SQ and HDH regions. Second, from the inset, we see that the QC12 is more stable than the AC12 even *without* the additional configurational entropy correction. This leads us to infer that the QC12 phase is stabilized by its vibrational entropy, i.e., the entropy associated with the number of configurations that the QC12 can probe by the vibrational motion of the particles around their lattice positions. This stems from the fact that the free energy calculated by the Frenkel-Ladd method has only two contributions, namely, the potential energy of the particles and their vibrational entropy, as stated in Eq. (12). Given that both the QC12 and AC12 have the same potential energy (for example, $U = E/\epsilon N = 2.536 \pm 0.02$ at

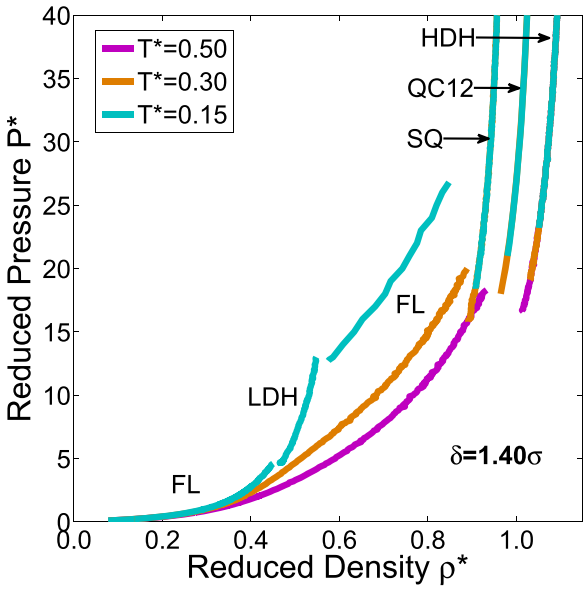

FIG. 5. Equations of state ($P^* = \beta P \sigma_{HD}^2$ versus $\rho^* = N\sigma_{HD}^2/A$) obtained for the HCSS system with $\delta = 1.40\sigma_{HD}$ and temperatures $T^* = k_B T/\epsilon = 0.15$, 0.30, and 0.50. The phases shown are fluid (FL), square (SQ), low-density (LDH), and high-density hexagonal (HDH) phase and a dodecagonal quasicrystal (QC12).

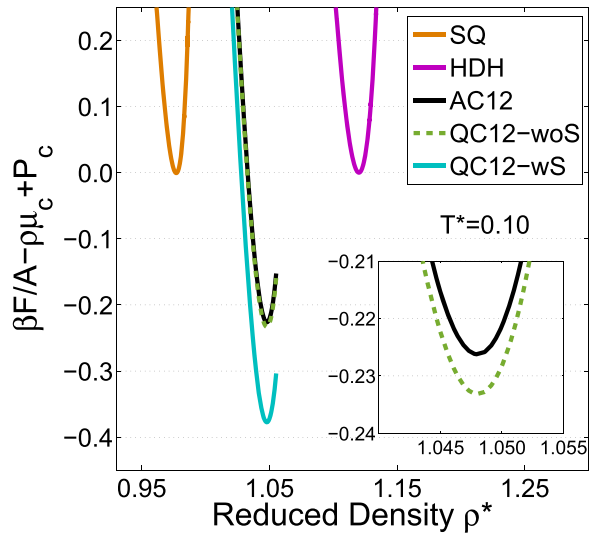

FIG. 6. Common tangent construction at the square-high-density hexagonal (SQ-HDH) phase coexistence obtained for the HCSS system with $\delta = 1.40\sigma_{HD}$ at reduced temperature $T^* = k_B T/\epsilon = 0.10$. The plot shows the Helmholtz free energy per unit area $\beta F/A$ as a function of reduced density $\rho^* = N\sigma_{HD}^2/A$. A linear fit $\rho\mu_c - P_c$ is subtracted from the free energy, where μ_c and P_c are the bulk chemical potential and bulk pressure at the (metastable) SQ-HDH phase coexistence. The phases shown are square (SQ), high-density hexagonal (HDH), crystalline approximant (AC12), and dodecagonal quasicrystal without (QC12-woS) and with the entropy correction (QC12-wS). Inset shows a closer look of the free energy curves of QC12-woS and AC12 phases.

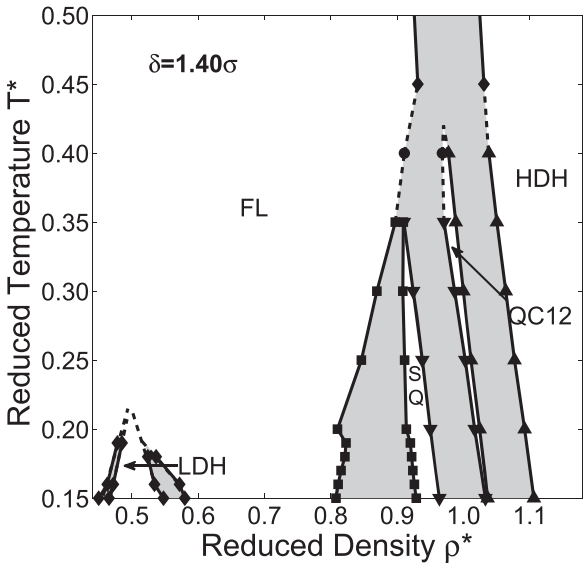

FIG. 7. Phase diagram in the (reduced) temperature-density representation obtained for the HCSS system with shoulder width $\delta = 1.40\sigma_{HD}$. The reduced quantities are defined as $T^* = k_BT/\epsilon$ and $\rho^* = N\sigma_{HD}^2/A$. The phases shown are fluid (FL), square (SQ), low-density (LDH), and high-density hexagonal (HDH) phase and the random-tiling dodecagonal quasicrystal (QC12). The grey regions denote the two-phase coexistence regions.

$\rho^* = 1.07$), the difference in the free energy is attributed to the vibrational entropy. This entropy pertaining to the vibrational motion of the particles is inherently calculated in the Frenkel-Ladd method by integrating the mean square displacements of the particles around their lattice sites as a function of the spring constant of the harmonic springs that tie the particles to their respective lattice positions. The higher vibrational entropy of the QC12 could be due to long-wavelength phonon contributions. However, we do not systemically study this aspect here. We also note that the QC12 is more stable than the AC12 irrespective of the additional configurational entropy contribution for the temperature range considered in this study. We speculate that the QC12 is more stable than the AC12 at even lower temperatures. At zero temperature, we contemplate that both QC12 and AC12 are equally stable considering their equal potential energy within our error bars. This has been addressed in more detail in our previous publication.[40]

Subsequently, we map out the phase diagram by performing the common tangent construction at various temperatures. The phase diagram in the reduced temperature-density ($T^* - \rho^*$) plane is given in Fig. 7. A preliminary version of this phase diagram was previously presented in Ref. 40. We present it here again to provide a comparison between the phase diagrams at three different shoulder widths. We make the following observations from the phase diagram. First, as noted from the EOS, a re-entrant fluid (FL) phase encompassing the low-density hexagonal (LDH) phase is found to be stable at low temperatures and densities. The LDH phase is formed with the particles separated from each other at a distance equal to the shoulder width. The stable close-packed phase is the high-density hexagonal (HDH) phase. At moderate densities, the square (SQ) phase is stabilized due to a lower energy, and the quasicrystal (QC12) with dodecagonal symmetry is sandwiched between the SQ and HDH phases at low temperatures and between the FL and HDH phases at high temperatures. Finally, we note that the phase boundaries hardly shift whether or not the additional configurational entropy term is taken into account as demonstrated in Ref. 40.

B. Shoulder width $\delta = 1.27\sigma_{HD}$

We now turn our attention to a HCSS system with shoulder width $\delta = 1.27\sigma_{HD}$, which exhibits the formation of an octadecagonal (18-fold symmetric) random-tiling quasicrystal (QC18) composed of rhombi and triangles as shown in Ref. 17. The structure is analogous to the dodecagonal quasicrystal (QC12) described in Section III A. Both tilings are constructed from three- and four-sided polygons. Whereas the four-sided polygon is a square in QC12 and a rhombus in QC18, the three-sided polygon is in both types of quasicrystals an equilateral triangle. All these polygons have sides of length σ_{HD}, whereas the rhombus in the QC18 is constructed such that the diagonals are equal to the shoulder width $\delta = 1.27\sigma_{HD}$. Fig. 8(a) shows a configuration of the QC18 obtained at $\rho^* = 0.98$ and $T^* = 0.20$ in the *NVT* ensemble. The particle configuration in the core-only representation is shown on the top which is coloured according to their LPEs described in Section II B. The bottom contains the rhombic-triangle tiling (left) and calculated diffraction pattern (right). Defects of predominately pentagonal shapes are observed, similar to the QC12.

Constructing the defect-free configuration and a crystalline approximant for this octadecagonal quasicrystal is not

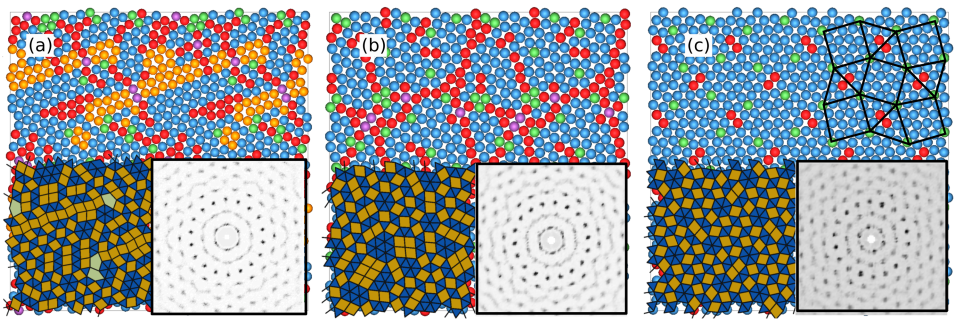

FIG. 8. The random-tiling octadecagonal quasicrystal (QC18) as obtained from simulations (a), a defect-free construction of a random-tiling QC18 (b), and a crystalline approximant (AC18) (c). Each figure displays a typical configuration (top), where the particles are shown in core-only representation and the colours represent the local particle environments (LPEs) as described in Fig. 2, along with its corresponding rhombus-triangle tiling (bottom left) and diffraction pattern (bottom right). The rhombus-triangle tiling formed by the centres of the distorted dodecagons in the approximant in (c) is highlighted.

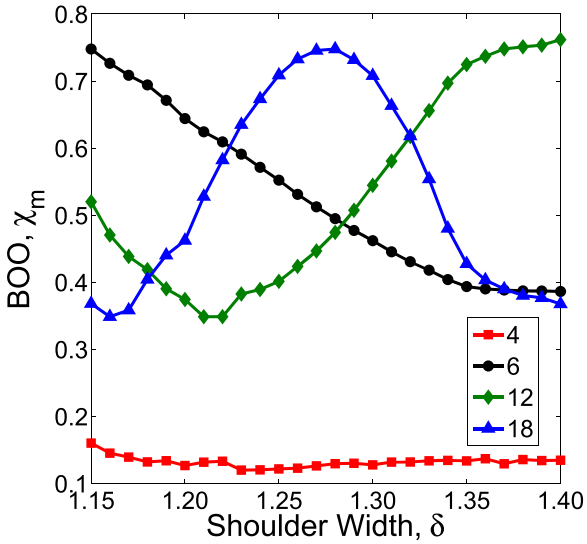

FIG. 9. The m-fold bond orientational order (BOO) parameter χ_m showing the formation of an octadecagonal quasicrystal (QC18) from a dodecagonal quasicrystal (QC12) in the HCSS system at temperature $T^* = k_BT/\epsilon = 0.20$ by reducing the shoulder width in a Monte Carlo simulation in the NVT ensemble.

straightforward as random rhombic-triangle tilings are not as widely studied as the square-triangle tilings. However, it has previously been observed that the QC18 can be formed from the QC12 by decreasing the temperature followed by gradually decreasing the shoulder width.[17] Here, we use a similar method to obtain the defect-free QC18 and AC18 by exclusively decreasing the shoulder width from $1.40\sigma_{HD}$ to $1.27\sigma_{HD}$ at a constant temperature $T^* = 0.20$. In Figs. 8(a) and 8(b), we present the resulting configurations of the defect-free QC18 and the AC18. The accompanying diffraction patterns affirm the 18-fold symmetry. In addition, we plot the 4-, 6-, 12-, and 18-fold BOO parameters as a function of the shoulder width in Fig. 9 to monitor the transformation from AC12 to AC18 at temperature $T^* = 0.20$. A decrease in χ_{12} accompanied by an increase in χ_{18} is observed upon decreasing the shoulder width δ from $1.40\sigma_{HD}$ to $1.27\sigma_{HD}$. Upon decreasing the shoulder width further, we find that both χ_{12} and χ_{18} decrease and χ_6 increases. From this behaviour, we establish the presence of a 18-fold symmetric phase in a range of shoulder widths between $1.23\ \sigma_{HD}$ and $1.32\sigma_{HD}$, bordered by a 12- and a 6-fold symmetric phase. We further call attention to the high value of χ_6 at these intermediate shoulder widths. This can also be noticed in the diffraction patterns in Figs. 8(b) and 8(c). This is due to the small system sizes used in this study. The system sizes used for QC18 and AC18 are the same as those of QC12 and AC12.

Given that the structures of the QC12 and QC18 quasicrystals are very similar, we also expect similar phase behaviour for both systems. The similarity in the phase behaviour is illustrated by the behaviour of the BOO parameters as a function of temperature and pressure in Fig. 10 and the EOS in Fig. 11. Analogous to the QC12, the QC18 is formed either by cooling of the hexagonal (HDH) phase to a lower temperature at constant density or by compressing the fluid (FL) phase to higher density at constant temperature. The behaviour of the BOO parameters χ_4, χ_6, and χ_{18} during these transformations is shown in Fig. 10. An increase in χ_{18} upon decreasing the temperature (Fig. 10(a)) or increasing the pressure (Fig. 10(b)) establishes the formation of the QC18 phase.

To construct the EOS, we used the rhombus (RH), the high-density hexagonal (HDH) phase, the approximant crystal (AC18), and the defect-free octadecagonal quasicrystal (QC18) as starting configurations for the expansion runs. We plot the EOS obtained at temperatures $T^* = 0.15$ and 0.40 in Fig. 11. Again, similar to the behaviour at $\delta = 1.40\sigma_{HD}$, the system displays hard-disk-like phase behaviour at high temperature and a re-entrant fluid followed by the formation of a quasicrystal at low temperature.

The point of deviation of the phase behaviour of the QC18 from the QC12 is the relative free energies of the quasicrystal and the approximant phases. We have previously seen that the QC12 has a lower free energy than the AC12 even without the entropy correction. The present case of QC18 and AC18 is illustrated by a common tangent construction between the RH and HDH phases (similar to Fig. 6). Fig. 12 shows this common tangent construction at $T^* = 0.20$. Similar to the previous case of QC12, we find that the QC18 and AC18 are more stable than the RH-HDH two-phase coexistence. On the other hand, we note from the inset that the difference in free energies between QC18 and AC18 is smaller than that between QC12 and AC12 and is of the order of the statistical error of the free energy. Thus, the relative stability of one over the other cannot be accurately established. Further, we find that at the close-packed density of $\rho^* = 1.07$, both AC18 and QC18 have a potential energy per particle $E/\epsilon N$ equal to 2.536 ± 0.002. Thus, the QC18 and the AC18 are approximately equally stable without the entropy correction, whereas any extra

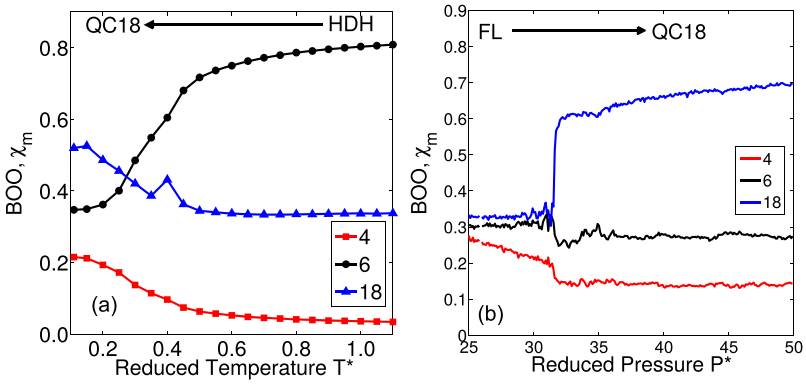

FIG. 10. The m-fold bond orientational order (BOO) parameter χ_m as a function of temperature T^* as obtained by cooling a high-density hexagonal (HDH) phase at density $\rho^* = N\sigma_{HD}^2/A = 0.98$ in a simulation of the HCSS system with $\delta = 1.27\sigma_{HD}$ in the NVT ensemble (a) and as a function of pressure P^* by compressing a fluid (FL) phase at temperature $T^* = k_BT/\epsilon = 0.30$ in the NPT ensemble (b).

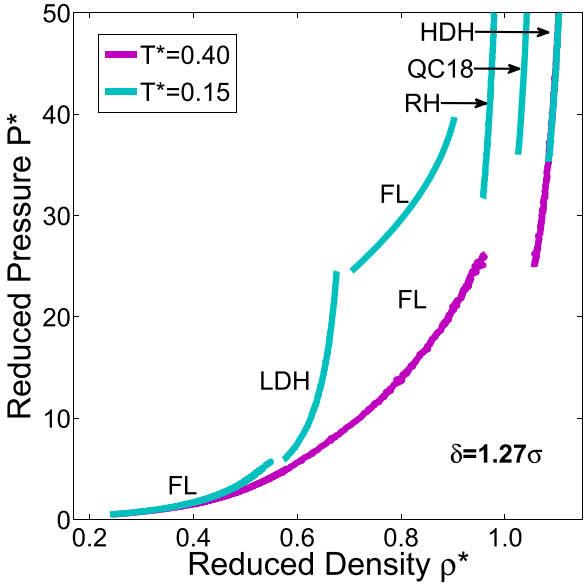

FIG. 11. Equations of state ($P^* = \beta P \sigma_{HD}^2$ versus $\rho^* = N\sigma_{HD}^2/A$) obtained for the HCSS system with $\delta = 1.27\sigma_{HD}$ and temperatures $T^* = k_BT/\epsilon = 0.15$ and 0.40. The phases shown are fluid (FL), rhombus (RH), low-density (LDH), and high-density hexagonal (HDH) phases and the random-tiling octadecagonal quasicrystal (QC18).

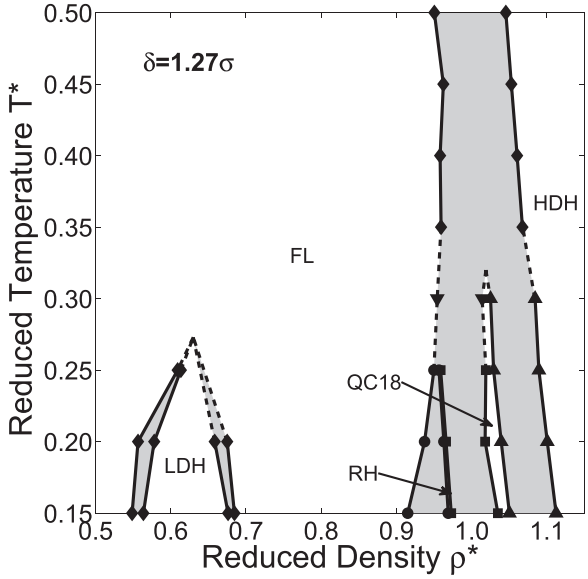

FIG. 13. Phase diagram in the (reduced) temperature-density representation obtained for the HCSS system with shoulder width $\delta = 1.27\sigma_{HD}$. The reduced quantities are defined as $T^* = k_BT/\epsilon$ and $\rho^* = N\sigma_{HD}^2/A$. The phases shown are fluid (FL), rhombus (RH), low-density (LDH), and high-density hexagonal (HDH) phases and the random-tiling octadecagonal quasicrystal (QC18). The grey regions denote the two-phase coexistence regions.

configurational entropy contribution arising from the number of distinct configurations of the QC18 stabilizes the QC18 over the AC18. We thus assume that the QC18 is more stable than the AC18.

The phase diagram was subsequently mapped out using the free energy of the QC18 phase with the configurational entropy contribution. We stress again that the shift in the phase boundaries is tiny whether or not the configurational entropy contribution is taken into account. Fig. 13 displays the phase diagram in the (reduced) temperature-density ($T^* - \rho^*$) plane. The low density-low temperature region ($T^* < 0.25$ and $\rho^* < 0.3$) of the phase diagram is represented by a re-entrant fluid (FL) engulfing the low-density hexagonal (LDH) phase. The LDH phase is formed with the particles separated from each other at a distance equal to the shoulder width $\delta = 1.27\sigma_{HD}$. The high temperature regime ($T^* \geq 0.35$) is characterized by a fluid at low densities and a high-density hexagonal (HDH) phase at high densities with the FL-HDH two-phase coexistence region in between. At low (or intermediate) temperatures, a stable QC18 region adjoined by a stable rhombus (or fluid) and a high-density hexagonal (HDH) phase is observed. The narrowness of the density regime of the stable rhombus phase is attributed to the geometric constraints enforced by the structure of the phase on the side lengths of the rhombi. This constraint does not allow the sides of the rhombi to change independently and thus does not accommodate large changes in densities.

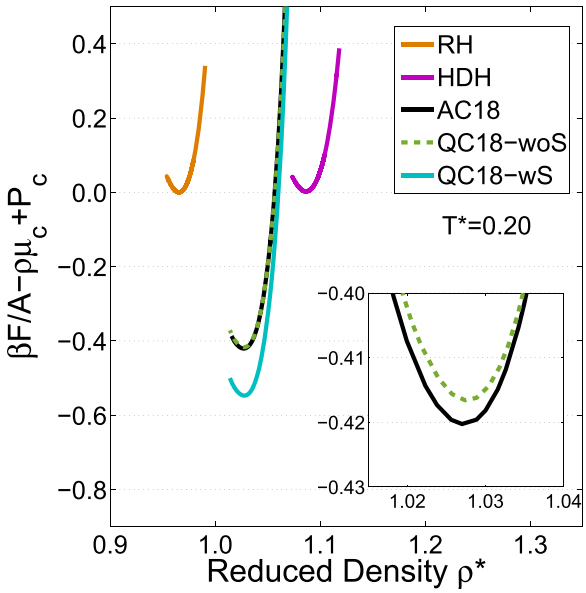

FIG. 12. Common tangent construction at the rhombus-high-density hexagonal (RH-HDH) phase coexistence obtained for the HCSS system with $\delta = 1.27\sigma_{HD}$ at reduced temperature $T^* = k_BT/\epsilon = 0.20$. The plot shows the Helmholtz free energy per unit area $\beta F/A$ as a function of reduced density $\rho^* = N\sigma_{HD}^2/A$. A linear fit $\rho\mu_c - p_c$ is subtracted from the free energy, where μ_c and P_c are the bulk chemical potential and bulk pressure at the (metastable) RH-HDH phase coexistence. The phases shown are rhombus (RH), high-density hexagonal (HDH) phase, crystalline approximant (AC18), and octadecagonal quasicrystal without (QC18-woS) and with the entropy correction (QC18-wS). Inset shows a closer look of the free energy curves of QC18-woS and AC18 phases.

C. Shoulder width $\delta = 1.60\sigma_{HD}$

Finally, we investigate a system consisting of HCSS particles with shoulder width $\delta = 1.60\sigma_{HD}$, where a random-tiling decagonal (10-fold symmetric) quasicrystalline (QC10r) phase was previously reported by Dotera *et al.*[17] The decagonal quasicrystal differs from the previous two quasicrystals on the basis of two factors, namely, density and tiling. First, the close-packed density ρ^* of QC12 and QC18 was 1.07, whereas the QC10r obtained in simulations had a density $\rho^* \approx 0.70$.[17] Second, in stark contrast to the two-member polygonal tilings of QC12 and QC18, the tiling of QC10r consists of a series of polygons with at least five sides. We show in Fig. 14(a) a typical

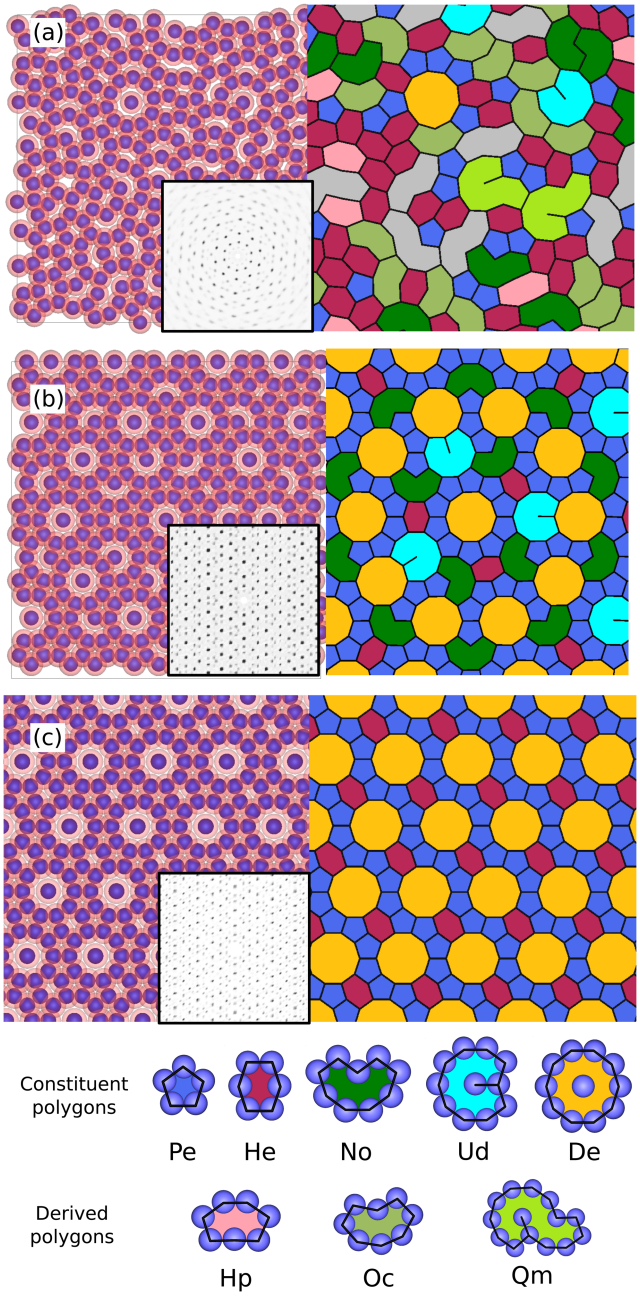

FIG. 14. Difference between (a) the random-tiling decagonal quasicrystal obtained in simulations (QC10r), (b) the constructed decagonal quasicrystal (QC10), and (c) the decagonal approximant (AC10). The particle configurations containing both the hard core and the soft shoulder of the particles are shown on the left. Their respective tilings are drawn on the right. Inset shows the calculated diffraction pattern. The legend of the constituent and derived polygonal tiles is given at the bottom.

configuration of a QC10r at $T^* = 0.20$ as obtained by cooling the HDH phase to a lower temperature at constant density $\rho^* = 0.70$. In the left figure, we show the particle configuration with both the hard core and soft corona. The inset shows the calculated diffraction pattern exhibiting decagonal symmetry. The accompanying tiling is drawn on the right. We see that the tiling is constituted by the following polygonal tiles: pentagon (Pe), hexagon (He), heptagon (Hp), octagon (Oc), nonagon (No), decagon (De), collapsed decagon (Ud), and question-mark (Qm). The polygonal tiles with more sides than the ones listed above are shaded in grey in Fig. 14(a). These tiles are

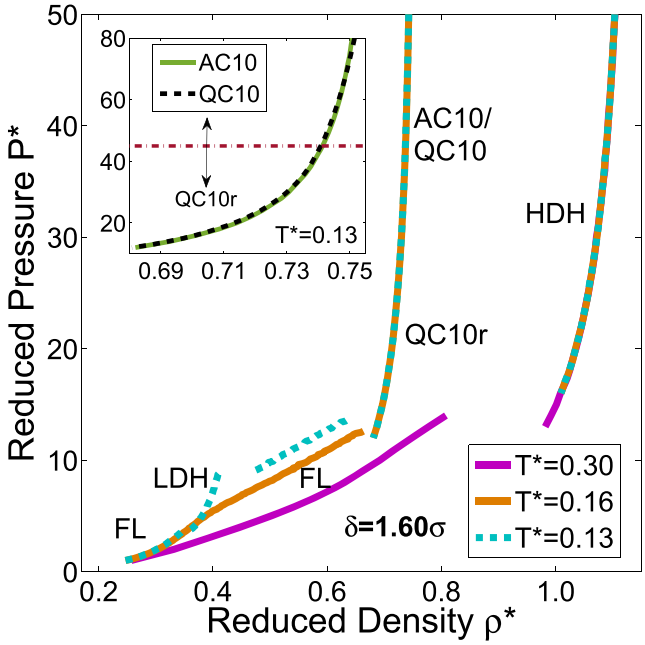

FIG. 15. Equations of state obtained for the HCSS system with $\delta = 1.60\sigma_{HD}$ and temperatures $T^* = k_BT/\epsilon = 0.13$, 0.16, and 0.30. The phases shown are fluid (FL), low-density (LDH) and high-density hexagonal (HDH) phases, a decagonal approximant (AC10), and a perfect (QC10) and a random-tiling decagonal quasicrystal (QC10r). The inset shows a zoomed in view of the equations of state of the AC10, QC10, and QC10r phases at $T^* = 0.13$. The dash-dot line here indicates the pressure below which the derived polygonal tiles start to form in these structures, corresponding to the QC10 (or AC10) to QC10r transition.

identified by keeping in mind the constituent tiles of commonly studied decagonal quasicrystals and approximants as described below.[9,11,32,42]

As in the previous cases of QC12 and QC18, we study the relative stability of QC10r with a perfect decagonal quasicrystal (QC10) and a decagonal approximant (AC10). The QC10 is adapted from a Mikulla–Roth binary tiling as a decoration of the Tübingen triangle tiling[42] and is shown in Fig. 14(b). It has a close-packed density of 0.7608. It is composed of 330 particles arranged into five constituent polygons; namely, Pe, He, No, De, and Ud tiles. The AC10, on the other hand, consists of decagons arranged in a rhombic super tiling[9] as shown in Fig. 14(c). We use a large system of 2028 particles such that a rectangular super cell can be carved out of the rhombic super tiling. It has a closed-packed density of 0.7617 and consists of Pe, He, and De tiles.

Comparing the tilings of the QC10r, QC10, and the AC10 in Fig. 14, it is obvious that the QC10r tiling is described by additional polygonal tiles than those in the QC10 and AC10. This polygonal tiling of the QC10r has previously been interpreted by constructing the five constituent polygons using two types of Robinson's triangles.[17] In that interpretation, these additional polygonal tiles are considered to be derived from combinations of the constituent polygonal tiles. Among these derived polygonal tiles, we explicitly mark the Hp, Oc, and Qm tiles, which appear frequently in the simulations. We do not categorise the other derived tiles which can be construed as tube-like polygons of various lengths. These are shaded in grey in Fig. 14(a).

We study the phase behaviour of this system by first constructing the EOS of the phases present at different temperatures. The expansion runs were started with the high-density hexagonal (HDH) phase, the decagonal quasicrystal (QC10), and the decagonal approximant (AC10). The QC10r phase is formed from the QC10 and AC10 phases at lower pressures. In Fig. 15, we show the EOS obtained at temperatures $T^* = 0.30$, 0.16, and 0.13. The fundamental behaviour of the system at this shoulder width is similar to that at $\delta = 1.40\sigma_{HD}$ and $1.27\sigma_{HD}$. Notably, we observe hard-disk-like behaviour at high temperature ($T^* = 0.30$) and the formation of a low-density hexagonal (LDH) phase at low temperature ($T^* = 0.13$). The difference appears at intermediate density ranges, especially in the EOS of the quasicrystal.

We find that the EOS of the QC10 and AC10 lies very close to each other. To analyse them in detail, we plot a closer view of their EOS at $T^* = 0.13$ in the inset of Fig. 15. We find that, at these conditions, the difference between the two EOSs is of the order of the statistical error in our calculation. Given that both these structures exhibit similar behaviour, we explain only that of the QC10 here. During the expansion of the QC10, we find that derived polygonal tiles start to form in order to accommodate the extra space in the structure due to a lower density. These local rearrangements of particles are accommodated by phason flips. For example, in Fig. 16, we present the tilings of a typical particle configuration at pressures $P^* = 46$ and 45 for a temperature $T^* = 0.13$. We clearly find that a tiling consisting of a Pe, Ud, and De tile rearranges into a tiling consisting of a Ud and a Qm tile. A closer look at this rearrangement is given in Fig. 16(c). Here the centre-of-mass of the particles is depicted along with their nearest-neighbour bonds. The particle positions at $P^* = 46$ are in grey and those at $P^* = 45$ are in blue. We also draw in red the vectors denoting the displacement of each particle between these two states.

The formation of the derived polygonal tiles essentially denotes a transition from the QC10 to the QC10r structure. However, we do not see any clear signature of this transition in the EOS as shown in Fig. 15. This indicates that the rearrangements in the tilings are required to accommodate the change in density, i.e., more open-derived polygons form at lower densities. Consequently, we consider QC10 and QC10r to be a single structure for further analysis.

The free energies of the FL, QC10, and AC10 phases were calculated according to the Schilling-Schmid method and that of the HDH phase using the Frenkel-Ladd method as explained in Section II D. The stable phases at each temperature were then calculated using common tangent constructions between each pair of phases. For example, Fig. 17 displays the relative stability of the phases at $T^* = 0.11$. Here, the chemical potential $\beta\mu$ of the phases as a function of pressure P^* is plotted. Two phases coexist when their respective chemical potentials are equal at a given pressure. This can be seen as a point of intersection between two curves in the $\beta\mu - P^*$ plot. The stability region of each phase is marked by arrows at the bottom of the figure. We individually mark the curves pertaining to the QC10 and AC10 phases, which lie on top of each other. Comparing the pressure range of formation of the QC10 (or AC10) phases with the EOS given in Fig. 15, we find that it corresponds to the region where the structure comprises derived polygonal tiles, i.e., the QC10r structure. Thus, we conclude that the stable phase with decagonal order in the system is QC10r. Ultimately, the order of stability of the phases at this temperature is found to be FL-LDH-FL-QC10r-HDH upon increasing the pressure P^*.

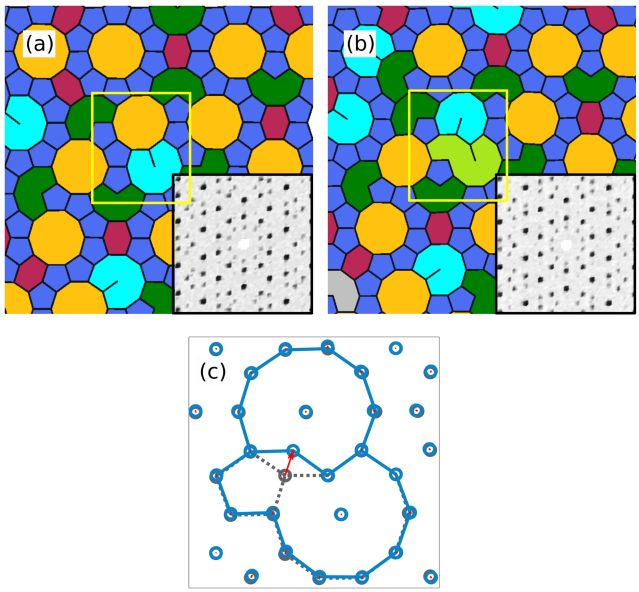

FIG. 16. Tilings of particle configurations obtained at pressures $P^* = \beta P\sigma_{HD}^2$ = (a) 46 (b) 45 at temperature $T^* = k_BT/\epsilon = 0.13$ showing the formation of derived polygonal tiles in the constructed decagonal quasicrystal (QC10) structure. The tiles are coloured according to the convention given in Fig. 14. Inset shows the calculated diffraction pattern. (c) A closer look at the tile rearrangement where the particles' positions at $P^* = 46$ are in grey and that at $P^* = 45$ are in blue. The displacement vectors are in red.

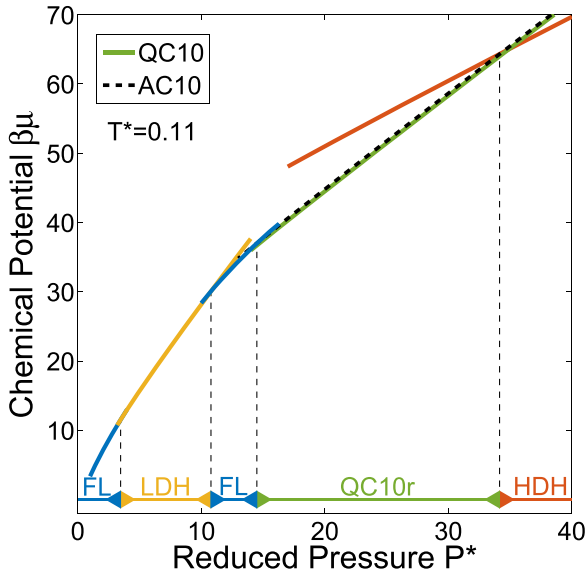

FIG. 17. The chemical potential $\beta\mu$ as a function of reduced pressure $P^* = \beta P\sigma_{HD}^2$ at temperature $T^* = k_BT/\epsilon = 0.11$ for the HCSS system with $\delta = 1.60\sigma_{HD}$. The stable phases are fluid (FL), low-density (LDH) and high-density hexagonal (HDH) phases, and random-tiling decagonal quasicrystal (QC10r) phase. The stability region of QC10r is obtained from the curves pertaining to the perfect decagonal quasicrystal (QC10) and its approximant (AC10). The arrows denote the phase stability regions.

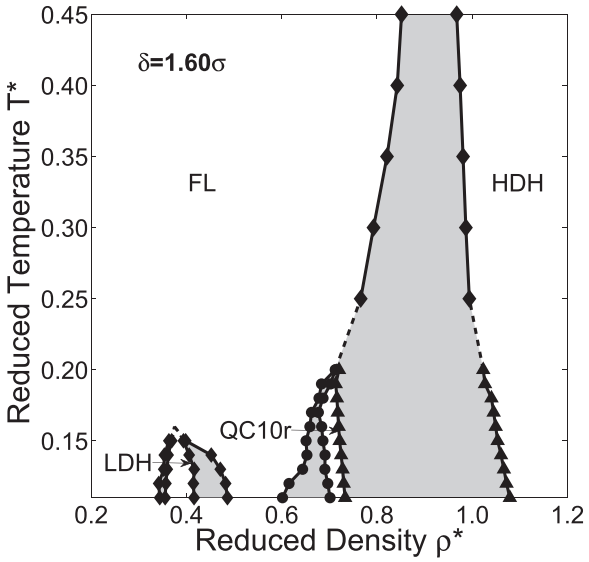

FIG. 18. Phase diagram in the (reduced) temperature-density representation obtained for the HCSS system with shoulder width $\delta = 1.60\sigma_{HD}$. The reduced quantities are defined as $T^* = k_BT/\epsilon$ and $\rho^* = N\sigma_{HD}^2/A$. The stable phases shown are fluid (FL), low-density (LDH) and high-density hexagonal (HDH) phases, and the random-tiling decagonal quasicrystal (QC10r) phase. The grey regions denote the two-phase coexistence regions.

In Fig. 18, we plot the phase diagram in the (reduced) temperature-density ($T^* - \rho^*$) plane. Similar to the previous two shoulder widths, the low-temperature low-density behaviour is characterised by re-entrant phase behaviour of the fluid (FL) phase encompassing the low-density hexagonal (LDH) phase. The stable phase at high densities is the high-density hexagonal (HDH). The quasicrystal (QC10r) is formed at intermediate densities at low temperatures ($T^* \leq 0.20$). We find that the maximum density of the stable QC10r phase is ≈0.73, whereby the structure always contains derived polygonal tiles. This essentially means that the QC10 and AC10, which solely consist of the constituent polygons, are not stable phases in this system. It is, however, interesting to note that stable QC10 and AC10 phases have previously been reported in a system of particles interacting with Lennard-Jones-Gauss potential.[32] The absence of QC10 (or AC10) in the HCSS system emphasises the strong dependence of the formation of a quasicrystal (or approximant) on the interaction potential.

IV. CONCLUSIONS

To summarise, we investigated the bulk phase behaviour of a system of colloidal particles interacting through a hard core and a purely repulsive square-shoulder pair potential for three different shoulder widths $\delta = 1.27\sigma_{HD}, 1.40\sigma_{HD}$, and $1.60\sigma_{HD}$. The system shows similar phase behaviour at low and high densities for all three shoulder widths. At low densities, the fluid exhibits a re-entrant phase behaviour circumscribing a low-density hexagonal (LDH) phase due to the presence of two length scales in the interaction potential. At high densities, a high-density hexagonal (HDH) phase is found to be stable. At intermediate densities, for $\delta = 1.40\sigma_{HD}$ and $1.27\sigma_{HD}$, a square and a rhombus phase are, respectively, observed. No crystalline phase is observed at intermediate density for $\delta = 1.60\sigma_{HD}$.

The most distinguished feature of the HCSS system is the formation of quasicrystals as reported by Dotera *et al.*[17] They demonstrated the formation of quasicrystals with different symmetry at different shoulder widths. An octadecagonal (18-fold symmetric) quasicrystal is formed at $\delta = 1.27\sigma_{HD}$, a dodecagonal (12-fold symmetric) quasicrystal at $\delta = 1.40\sigma_{HD}$, and a decagonal (10-fold symmetric) quasicrystal at $\delta = 1.60\sigma_{HD}$. Here, we investigated the thermodynamic stability of these quasicrystals with respect to a disordered fluid phase, periodic crystal phases, and periodic approximants. To this end, we calculate the free energy of the dodecagonal and octadecagonal quasicrystals using the Frenkel-Ladd method and add an extra contribution pertaining to the configurational entropy. For the decagonal quasicrystal, we employ the Schilling-Schmid method to calculate the free energy. We find that the dodecagonal quasicrystal is stabilised over its approximant even without the entropy correction for a HCSS system at shoulder width $\delta = 1.40\sigma_{HD}$. On the contrary, the octadecagonal quasicrystal without the entropy correction and its approximant were equally stable without the entropy correction for a HCSS system at shoulder width $\delta = 1.27\sigma_{HD}$. However, any configurational entropy contribution associated with the number of distinct configurations of the octadecagonal quasicrystal phase will stabilise it over its approximant. We thus assume that the octadecagonal quasicrystal phase will be more stable than the approximant. In the case of the decagonal quasicrystal, we find that the approximant is not stable at the densities where the quasicrystal is formed for a HCSS system at shoulder width $\delta = 1.60\sigma_{HD}$. In conclusion, we have mapped out the phase diagrams of HCSS systems for three different shoulder widths. We show that the phase diagrams display stable regions of the decagonal, dodecagonal, and octadecagonal quasicrystal phases. We also stress that the phase boundaries are insensitive whether or not the configurational entropy term is included corresponding to the number of distinct QC configurations.

Finally, we mention that we do not consider the other 18-fold ($\delta = 1.43\sigma_{HD}$) and 24-fold ($\delta = 1.29\sigma_{HD}$) quasicrystalline phases reported at densities just above that of the LDH by Dotera *et al.*[17] as their reported temperatures of formation ($T^* \sim 0.09$) are outside the temperature range of this study ($0.15 \leq T^* \leq 0.50$).

ACKNOWLEDGMENTS

This work is part of the Industrial Partnership Programme "Computational Sciences for Energy Research" (Grant No. 12CSER004) of the Foundation for Fundamental Research on Matter (FOM), which is part of the Netherlands Organisation for Scientific Research (NWO). This research programme is co-financed by Shell Global Solutions International B.V. We thank Wessel S. Vlug for helping with the tiling calculations and Simone Dussi and Guido Avvisati for critical reading of the manuscript.

[1] T. Dotera, Isr. J. Chem. **51**, 1197 (2011).
[2] D. Shechtman and I. Blech, Phys. Rev. Lett. **53**, 1951 (1984).
[3] X. Zeng, G. Ungar, Y. Liu, V. Percec, A. E. Dulcey, and J. K. Hobbs, Nature **428**, 157 (2004).

[4]A. Takano, W. Kawashima, A. Noro, Y. Isono, N. Tanaka, T. Dotera, and Y. Matsushita, J. Polym. Sci., Part B: Polym. Phys. **43**, 2427 (2005).
[5]T. Dotera and T. Gemma, Philos. Mag. **86**, 1085 (2006).
[6]K. Hayashida, T. Dotera, A. Takano, and Y. Matsushita, Phys. Rev. Lett. **98**, 195502 (2007).
[7]S. Lee, M. J. Bluemle, and F. S. Bates, Science **330**, 349 (2010).
[8]S. Fischer and A. Exner, Proc. Natl. Acad. Sci. U. S. A. **108**, 1810 (2011).
[9]M. Engel and H. Trebin, Phys. Rev. Lett. **98**, 225505 (2007).
[10]M. Engel, Ph.D. thesis, Universitat Stuttgart, 2008.
[11]M. Engel, M. Umezaki, H. R. Trebin, and T. Odagaki, Phys. Rev. B **82**, 134206 (2010).
[12]A. Skibinsky, S. V. Buldyrev, A. Scala, S. Havlin, and H. E. Stanley, Phys. Rev. E. **60**, 2664 (1999).
[13]D. Salgado-blanco and C. I. Mendoza, Soft Matter **11**, 889 (2015).
[14]L. Q. Costa Campos, C. C. de Souza Silva, and S. W. S. Apolinario, Phys. Rev. E **86**, 051402 (2012).
[15]M. Engel, P. F. Damasceno, C. L. Phillips, and S. C. Glotzer, Nat. Mater. **14**, 109 (2014).
[16]E. A. Jagla, Phys. Rev. E **58**, 11 (1998).
[17]T. Dotera, T. Oshiro, and P. Ziherl, Nature **506**, 208 (2014).
[18]H. G. Schoberth, H. Emmerich, M. Holzinger, M. Dulle, S. Förster, and T. Gruhn, Soft Matter **12**, 7644 (2016).
[19]A. Metere, M. Dzugutov, and S. Lidin, Soft Matter **12**, 8869 (2016).
[20]A. J. Archer, A. M. Rucklidge, and E. Knobloch, Phys. Rev. Lett. **111**, 165501 (2013).
[21]R. E. Ryltsev, B. A. Klumov, and N. M. Chtchelkatchev, Soft Matter **11**, 6991 (2015).
[22]R. Lifshitz and H. Diamant, Philos. Mag. **87**, 3021 (2007).
[23]K. Barkan, H. Diamant, and R. Lifshitz, Phys. Rev. B **83**, 172201 (2011).
[24]T. Dotera, J. Polym. Sci., Part B: Polym. Phys. **50**, 155 (2012).
[25]C. V. Achim, M. Schmiedeberg, and H. Löwen, Phys. Rev. Lett. **112**, 255501 (2014).
[26]P. Ziherl and R. D. Kamien, Phys. Rev. Lett. **85**, 3528 (2000).
[27]P. Ziherl and R. D. Kamien, J. Phys. Chem. B **105**, 10147 (2001).
[28]C. I. Mendoza and E. Batta, Europhys. Lett. **85**, 56004 (2009).
[29]A. Haji-Akbari, M. Engel, A. S. Keys, X. Zheng, R. G. Petschek, P. Palffy-Muhoray, and S. C. Glotzer, Nature **462**, 773 (2009).
[30]A. Haji-Akbari, M. Engel, and S. C. Glotzer, J. Chem. Phys. **135**, 194101 (2011).
[31]A. Haji-Akbari, M. Engel, and S. C. Glotzer, Phys. Rev. Lett. **107**, 215702 (2011).
[32]A. Kiselev, M. Engel, and H. R. Trebin, Phys. Rev. Lett. **109**, 225502 (2012).
[33]A. I. Goldman and R. F. Kelton, Rev. Mod. Phys. **65**, 213 (1993).
[34]C. R. Iacovella, A. S. Keys, and S. C. Glotzer, Proc. Natl. Acad. Sci. U. S. A. **108**, 9 (2011).
[35]D. Frenkel and B. Smit, *Understanding Molecular Simulation: From Algorithm to Applications* (Academic Press, 1996), ISBN: 0-12-267351-4.
[36]C. Vega, E. Sanz, J. L. F. Abascal, and E. G. Noya, J. Phys.: Condens. Matter **20**, 153101 (2008).
[37]M. Widom, Phys. Rev. Lett. **70**, 2094 (1993).
[38]T. Schilling and F. Schmid, J. Chem. Phys. **131**, 231102 (2009).
[39]F. Schmid and T. Schilling, Phys. Procedia **4**, 131 (2010).
[40]H. Pattabhiraman, A. P. Gantapara, and M. Dijkstra, J. Chem. Phys. **143**, 164905 (2015).
[41]J. Roth and F. Gähler, Eur. Phys. J. B **6**, 425 (1998).
[42]U. Koschella, F. Gähler, J. Roth, and H. R. Trebin, J. Alloy. Compd. **342**, 287 (2002).
[43]H. Weber, D. Marx, and K. Binder, Phys. Rev. B **51**, 14636 (1995).
[44]M. N. van der Linden, J. P. K. Doye, and A. A. Louis, J. Chem. Phys. **136**, 054904 (2012).
[45]A. Santos, M. Lopez de Haro, and S. Bravo Yuste, J. Chem. Phys. **103**, 4622 (1995).
[46]J. M. Polson, E. Trizac, S. Pronk, and D. Frenkel, J. Chem. Phys. **112**, 5339 (2000).
[47]A. M. Almudallal, S. V. Buldyrev, and I. Saika-Voivod, J. Chem. Phys. **137**, 034507 (2012).
[48]W. Li, H. Park, and M. Widom, J. Stat. Phys. **66**, 1 (1992).
[49]B. Nienhuis, Phys. Rep. **301**, 271 (1998).
[50]M. Oxborrow and C. L. Henley, Phys. Rev. B **48**, 6966 (1993).
[51]J. de Gier and B. Nienhuis, J. Stat. Phys. **87**, 415 (1997).
[52]M. T. Marechal, *Anisotropic Colloids: Bulk Phase Behavior and Equilibrium Sedimentation* (Utrecht University, 2009).
[53]D. Gratias, M. Quiquandon, and A. Katz, World Sci. **2000**, 1–72 (2002).
[54]M. O'Keeffe and M. M. J. Treacy, Acta Crystallogr., Sect. A: Found. Crystallogr. **66**, 5 (2010).